Improvement of Airflow Simulation by Refining the Inflow Wind Direction and Applying Atmospheric Stability for Onshore and Offshore Wind Farms Affected by Topography

Takakuwa, Susumu
Japan Renewable Energy Corporation

Uchida, Takanori
Research Institute for Applied Mechanics(RIAM), Kyushu University

https://hdl.handle.net/2324/5208223

出版情報：Energies. 15 (14), pp.5050-, 2022-07-11. MDPI (Multidisciplinary Digital Publishing Institute)
バージョン：

energies

MDPI

Article

Improvement of Airflow Simulation by Refining the Inflow Wind Direction and Applying Atmospheric Stability for Onshore and Offshore Wind Farms Affected by Topography

Susumu Takakuwa [1,*] and Takanori Uchida [2]

[1] Japan Renewable Energy Corporation, Roppongi Hills North Tower 10F, 6-2-31 Roppongi, Minato-ku, Tokyo 106-0032, Japan
[2] Research Institute for Applied Mechanics (RIAM), Kyushu University, 6-1 Kasuga-kouen, Kasuga, Fukuoka 816-8580, Japan; takanori@riam.kyushu-u.ac.jp
* Correspondence: stakakuwa@jre.co.jp; Tel.: +81-80-2279-0234; Fax: +81-3-6455-4897

Abstract: For this study, the annual frequency of atmospheric stability and the effects of topography were investigated, using ERA5 data and data from wind observation masts installed at four locations on an island for a site under development, where bidding will soon begin. As a result, we found that a variety of atmospheric stabilities appeared at the site, and that the annual average events were not neutral but, instead, unstable. Moreover, the deviation from neutral varied depending on wind direction and the wind speed varied greatly, depending on the mast position and wind direction. Additionally, it was necessary to reproduce the wind flow separation due to topography, in order to predict the wind conditions of wind turbines located close to the island. The accuracy of the airflow simulation by large eddy simulation was validated using the mast-to-mast wind speed ratio. For simulations, we used the commercial software RIAM-COMPACT, which has been widely used in Japan, as it allows the atmospheric stability to be freely set. As a result, we found that the accuracy could be improved by refining the inflow wind direction and taking the average of the results calculated under several atmospheric stability conditions.

Keywords: wind farm; large eddy simulation; topography; inflow direction; atmospheric stability

check for updates

Citation: Takakuwa, S.; Uchida, T. Improvement of Airflow Simulation by Refining the Inflow Wind Direction and Applying Atmospheric Stability for Onshore and Offshore Wind Farms Affected by Topography. *Energies* **2022**, *15*, 5050. https://doi.org/10.3390/en15145050

Academic Editors: Rafael Campos Amezcua and Erasmo Cadenas

Received: 30 May 2022
Accepted: 8 July 2022
Published: 11 July 2022

1. Introduction

The main purpose of this study is to improve airflow simulations for wind resource assessments of onshore and offshore wind farms affected by topography. In recent years, there has been high demand for the development of renewable energy, both in Japan and abroad, and bidding for offshore wind power projects has begun in Japan [1]. In Europe, many offshore wind power sites have already been installed; however, in order to accelerate the introduction of offshore wind power in Japan, Japan's unique problems must be addressed. In general, European offshore sites are located more than 10 km from the coast whereas, in Japan, planned offshore sites are expected to be located only a few kilometers from the coast, as the water depth quickly deepens a few kilometers off the coast. As a result, the sites are strongly influenced by the onshore topography and the wind speed distribution within the site is not uniform. Consequently, the turbulence intensity may be higher than that at European offshore sites. In addition, it is well-known that airflow separation due to topography is affected by atmospheric stability [2–7], but there have been very few studies on how atmospheric stability affects airflow separation due to the topography at onshore and nearshore sites in Japan. Atmospheric stability varies by country, region, and season.

Meteorological models, such as WRF (Weather Research Forecasting) [8], are generally adopted for analyses considering atmospheric stability; however, these models cannot reproduce complex airflows caused by topographic undulations, as their grid resolution is too large. In general, steady-state engineering models using Reynolds-averaged modeling (RANS) are employed for turbulence modeling at complex terrain sites, but the models have problems reproducing complex flows such as airflow separation and vortices [9]. In addition, the atmospheric stability is often assumed to be neutral. In recent years, nonlinear, unsteady flow analyses have become possible as a result of the rapid improvement of computers. A representative approach for such wind flow analyses uses a numerical turbulence model called large-eddy simulation (LES). In order to address the above-mentioned problems specific to Japan and improve the prediction of airflow through simulation, unsteady engineering models using LES as a turbulence model with appropriate atmospheric stability settings are required.

When an engineering model is used to predict annual energy production, instead of a meteorological model, the analysis is usually performed using 12 or 16 wind direction sectors; however, there is also a problem with dividing the wind direction. For example, when using 16 wind directions, a wind direction width of 22.5 degrees must be considered. In complex terrain, a 22.5 degree change in wind direction will alter the upwind terrain and, thus, the airflow characteristics, but applying an airflow simulation to a single wind direction in the sector is equivalent to assuming that there is no airflow change within a 22.5 degree wind direction width. For both nearshore and onshore sites, it is necessary to consider the atmospheric stability and devise an appropriate wind direction division scheme in order to accurately reproduce the effects of the terrain.

In this study, we examine the accuracy of airflow simulations with multiple atmospheric stability conditions by refining the inflow wind direction for the Saikai–Enoshima Island site in Japan [10,11], where the bidding will soon begin. First, the annual frequency of atmospheric stability and the effect of topography on the airflow were investigated using observations from four wind observation masts located on the island, along with ERA5 [12] data from the European Centre for Medium-Range Weather Forecasts. As a result, we found that various conditions of atmospheric stability appeared at the site, and that the annual average events were not neutral but biased towards being unstable or stable, depending on the wind direction. It was also found that a variety of mast-to-mast wind speed ratios existed in the same wind direction sector and that the numerical simulations for each of the 16 wind direction sectors, assuming atmospheric stability as being neutral, did not correspond to reality.

In order to match reality as much as possible, we propose a method that analyzes not only the central wind direction of the 16 wind direction sectors but also those at +11 degrees and −11 degrees, taking into account their annual frequency of occurrence. Furthermore, the proposed method averages the results of simulations considering multiple atmospheric stability conditions. The simulation software used was RIAM-COMPACT [3,9,13–16], a commercially available software widely used in Japan, which can perform unsteady simulations using LES and allows for freely setting the atmospheric stability, according to the Ri number. Airflow simulations were performed using the following methods: (A) the conventional method, where only the central wind direction in the 16 wind direction sectors was calculated with neutral atmospheric stability; (B) a method where multiple atmospheric stability conditions were set for the central wind direction, and the average of the results for these airflow simulations was taken; (C) a method where only neutral atmospheric stability was set, but the average of the airflow simulations in three wind directions (the central wind direction, +11 degrees, and −11 degrees) was taken; and (D) the proposed method, where the average was taken over the airflow simulations in three wind directions considering multiple atmospheric stability conditions. For example, with a set of four atmospheric stability cases, the proposed method (D) averages 12 airflow simulations. With respect to the evaluation of the numerical simulations, first, the variation of the vertical wind speed profile with atmospheric stability was examined. Second, the change in the mast-to-mast wind speed ratio with respect to changes in atmospheric stability and wind direction was examined. Next, by comparing four methods with respect to the accuracy of the prediction of the mast-to-mast wind speed ratio, the effect of refining the inflow wind direction and applying atmospheric stability was validated. Finally, changes in airflow patterns due to atmospheric stability were discussed. Although many researchers have conducted airflow simulations using LES for wind power generation [4,17,18], few have quantitatively evaluated the impact of both refining inflow wind direction and atmospheric stability on the accuracy of wind speed prediction for the purpose of wind resource assessment in complex terrain sites, which is the novelty of this study. In particular, flow field prediction techniques that can be validated with mast-to-mast wind speed ratios are extremely important for new wind power developments.

2. Overview of the Investigated Site

Figure 1 shows a general view of the site investigated in the present study. The site is located in the ocean off Nagasaki Prefecture, western Japan, about 10 km from the Goto Islands and 20 km from the Nishisonogi Peninsula; there is no conspicuous land around the site. An enlarged view of the area within the black frame in Figure 1 is shown in Figure 2, and a topographic map of the site is shown in Figure 3. The island, Enoshima, has an undulating topography of 2 km from east to west and 3 km from north to south, and the highest elevation is 139 m in the northern part of the island. There are four wind observation masts on the island (A, B, C and D), and we used data from a period when all four masts were observed at the same time during the year. Cup anemometers and wind vanes were installed at 58 m, 50 m and 40 m of the masts, and the observation systems were designed according to MEASNET guidelines [19] and IEC 61400-12-1 [20]. The topography of Enoshima Island is very complicated but, as the island is surrounded by the sea, the area is presumed to be more affected by atmospheric stability, which is closely related to the surrounding sea surface temperature, rather than general land sites. As general airflow simulations were performed for each of the 12 to 16 wind direction sectors, the accuracy of this study was validated for six wind direction sectors—N, NNE, S, SSW, NW, and NNW—based on their frequency of occurrence.

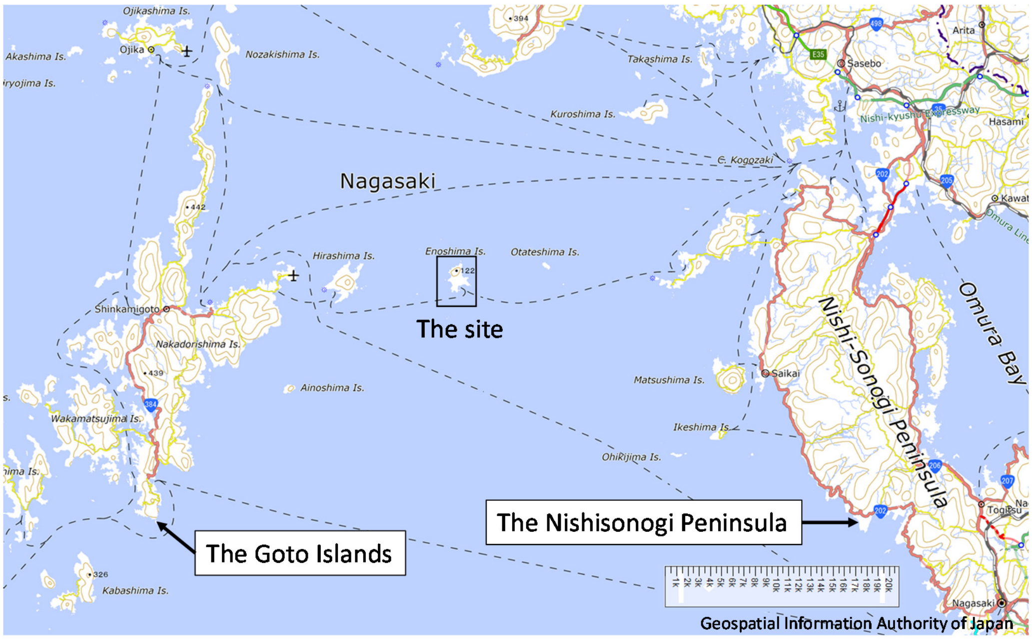

Figure 1. Overview of the site considered in this study. The name of the island is Enoshima.

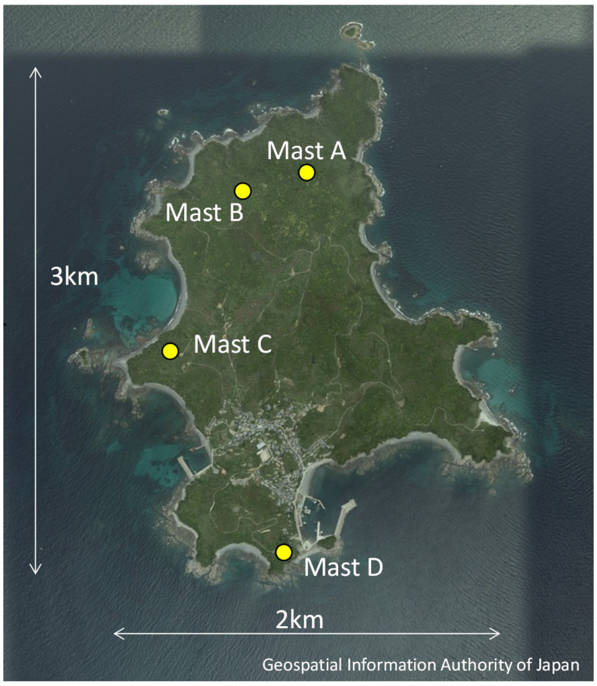

Figure 2. Enlarged view of the site within the black frame in Figure 1. There are four wind observation masts located on the island (A, B, C and D).

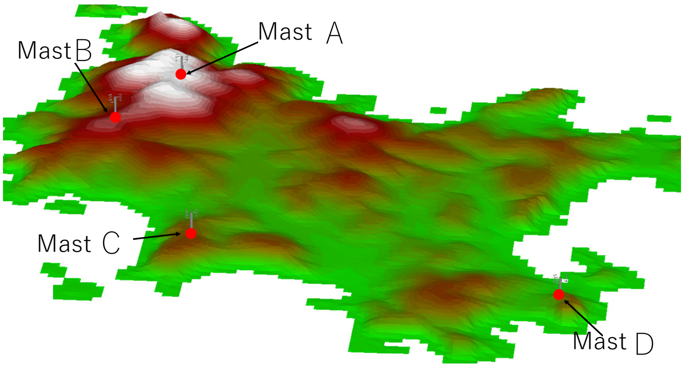

Figure 3. Terrain map of Enoshima Island.

3. Analysis of the Measurement Data

3.1. Correlation and Wind Speed Ratio for Each Mast

First, the correlation and wind speed ratios for each mast were assessed. In order to determine a stable wind speed relationship between the masts, a 1-hour average was used. In this study, the measured wind speed ratios were analyzed in detail for the north wind, which is greatly affected by the terrain. The details are discussed later, but this confirmed that the wind speed ratios of Masts B, C and D were significantly different in the north wind simulation. Moreover, the measured turbulence intensity of the north wind at Mast A was the highest among the turbulence intensities for each of the 16 wind direction sectors for all masts. Figure 4 shows the wind speed correlations and wind speed ratios for Masts B, C and D, relative to Mast A. The wind speed of Mast B was higher than that of Mast A, while the wind speeds of Masts C and D were lower than that of Mast A. All masts were well-correlated, but there was a great deal of variability in the wind speed ratios. At high wind speed, the wind speed ratio of mast B showed lower variability, but there was still considerable variability in C and D. A single-case airflow simulation adopting a conventional method calculates a single wind speed ratio, but that does not correspond to reality as various wind speed ratios may be observed, such as was the case at this site. The reason for the occurrence of various wind speed ratios is presumed to be the occurrence of various atmospheric stabilities and the influence of the terrain, which is not uniform over the 22.5 degree range. Therefore, it is necessary to perform simulations in accordance with this fact for accurate wind resource assessments.

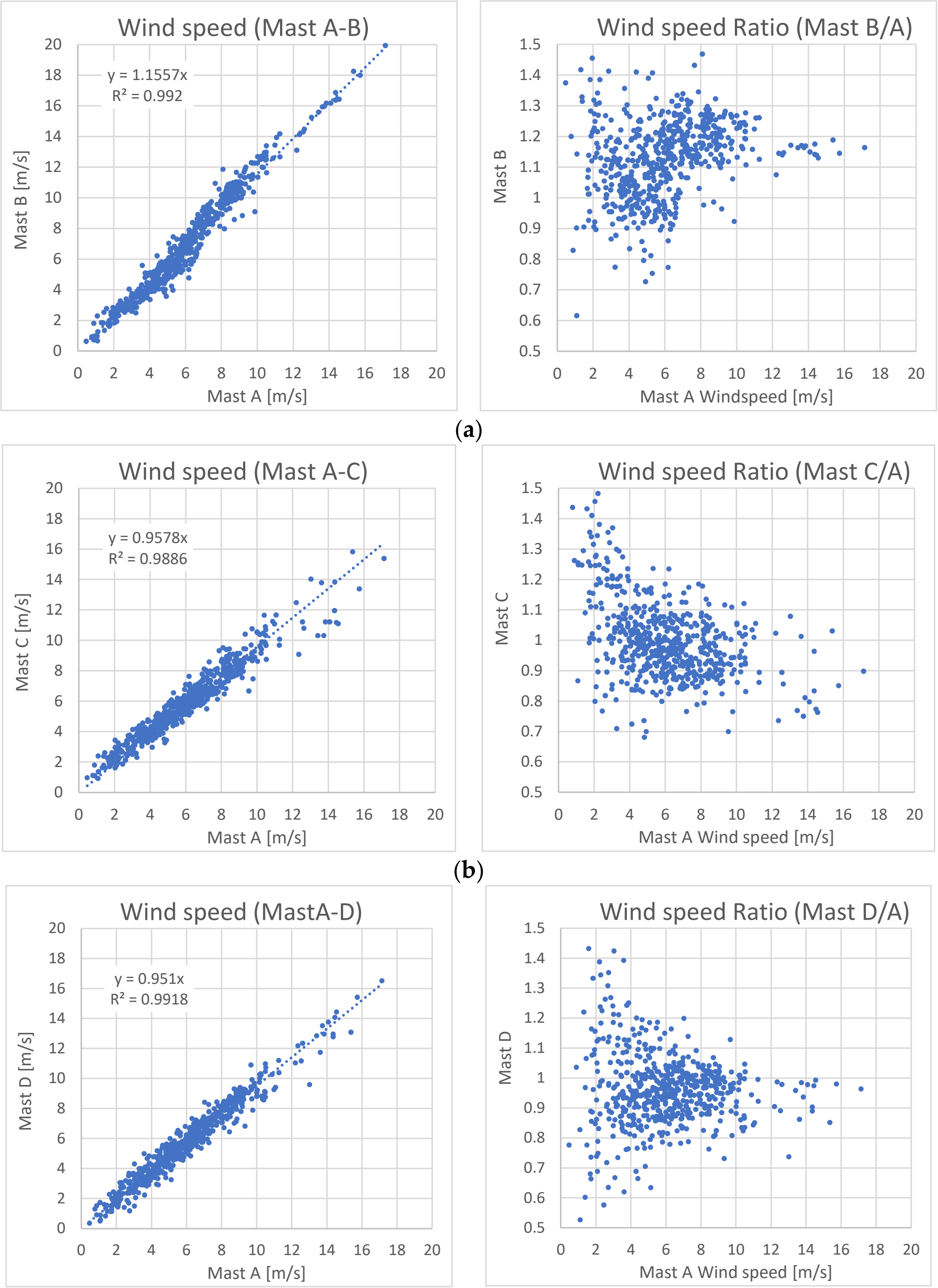

(**a**)

(**b**)

(**c**)

Figure 4. Correlation and wind speed ratios for: Mast A (**a**); Mast B with respect to A; (**b**) Mast C with respect to A; and (**c**) Mast D with respect to A.

3.2. Distribution of Annual Atmospheric Stability

Next, we examined the effect of atmospheric stability on the site wind conditions. The atmospheric stability is defined by the Richardson number (Ri), using the following equation:

$$\mathrm{Ri} = \frac{\mathrm{g}(\theta_{\mathrm{in}} - \theta_{\mathrm{bottom}})\,\mathrm{h}}{\theta_{\mathrm{in}}\mathrm{U}^2}, \tag{1}$$

where g is the gravitational acceleration; h is the maximum elevation difference at the site; θ_{in} is the temperature observed at Mast A, which is generally located near the maximum elevation at the site; θ_{bottom} is the sea surface temperature obtained from ERA5; and U is the 58 m altitude wind speed at Mast A. Ri = 0 indicates neutral atmospheric stability, a negative value indicates an unstable condition, and a positive value indicates a stable condition.

The annual frequency for the occurrence of atmospheric stability in the north wind is shown in Figure 5. The atmospheric stability was widely distributed from unstable to stable, but values above +1 or below −1 occurred at low wind speeds. The median value was slightly biased toward unstable conditions, contributed to by the fact that the sea surface temperature around the site located in western Japan is relatively warm. The relationship between the variability of atmospheric stability and wind speed is shown in Figure 6. As the wind speed increased, the variation in Ri converged. Although atmospheric stability is generally considered to be neutral at high wind speeds, it was slightly biased toward unstable conditions, even at wind speeds above 12 m/s, at which point the variation in Ri converged.

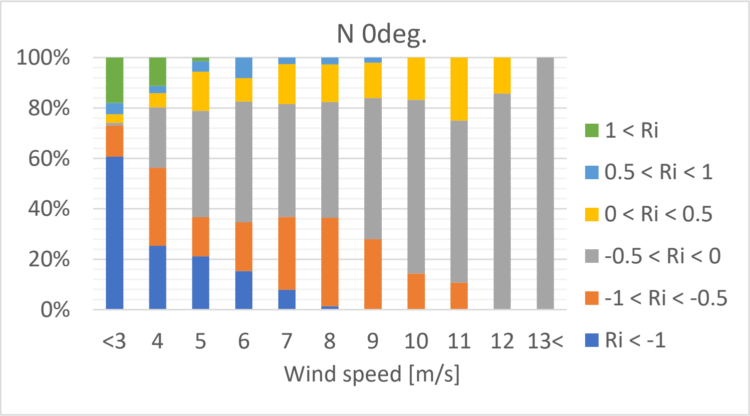

(**a**)

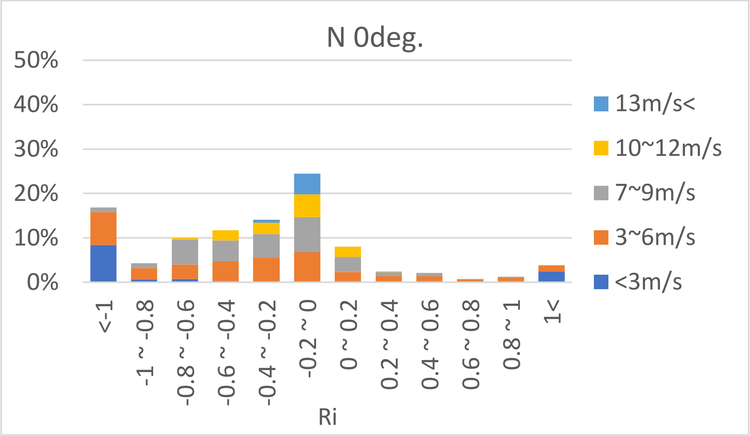

(**b**)

Figure 5. Annual frequency of occurrence of atmospheric stability in the north wind: (**a**) Percentage for each wind speed bin; and (**b**) percentage of each Ri bin for all data.

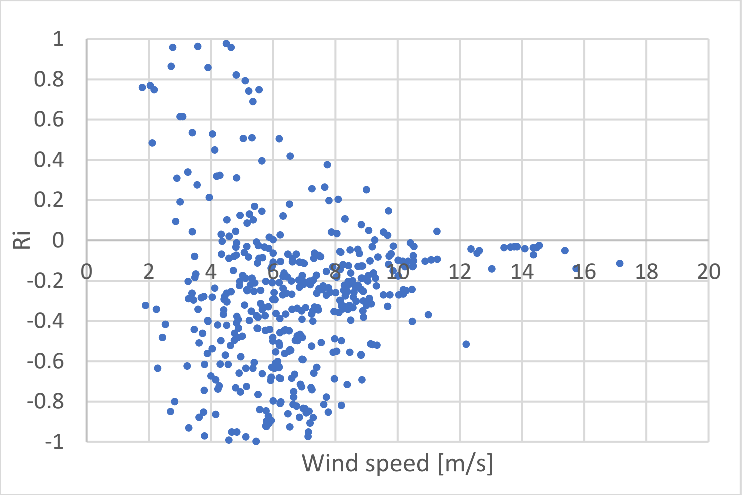

Figure 6. Relation between wind speed and atmospheric stability (Ri).

3.3. Investigation in Relation to the Variation of Atmospheric Stability

The relationship between the wind speed ratio and atmospheric stability Ri is shown in Figure 7. We expected to see some relation between atmospheric stability and the wind speed ratio, but variation in the wind speed ratio was still large without any relation to the atmospheric stability.

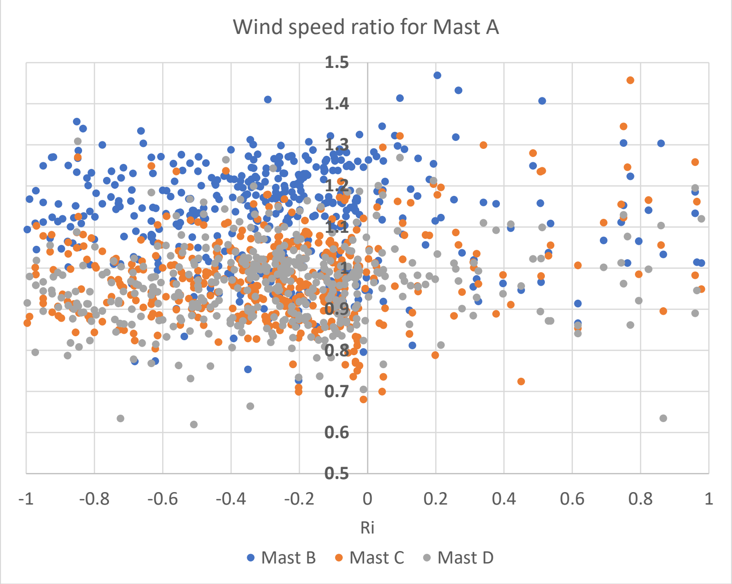

Figure 7. Relation between the wind speed ratios for Masts B, C and D with respect to A and the atmospheric stability Ri.

Figure 8 shows time-series data for the wind speed ratios and atmospheric stability; a time when only the north wind continued to blow for as long as possible was selected. The wind speed ratios on July 5 (Figure 8a) and July 15 (Figure 8b) fluctuated, to some extent, in conjunction with the upward and downward movements of Ri, but the linkage was not clear, as there were time gaps. In both cases, the wind speed ratio fluctuated above or below 1.0, although the atmospheric stability was consistently in an unstable condition. In other words, the trend of a higher or lower wind speed (compared to Mast A) was reversed under the continuous conditions of unstable atmospheric stability and north wind around 8 m/s. From these results, it can be inferred that the wind speed ratio in the time-series was somewhat affected by atmospheric stability, but other significant factors also exist. In this study, the atmospheric stability was set based on the temperature difference between the sea surface temperature and the site air temperature, assuming that the temperature of the inflow was uniform in the vertical direction. However, in reality, various temperature distributions occur in the vertical direction, and the influence of topography is not uniform within the 22.5 degree width of the wind direction sector N. In reality, a wide variety of winds cannot be classified by the azimuthal classification of north wind and the atmospheric stability given by Equation (1). While it is impractical to calculate all the various wind conditions when predicting energy production in wind power projects, the conventional method of calculating only neutral cases for the central wind directions of each of the 16 wind direction sectors is not always capable of reproducing intermediate or average events with wind speed ratios that seem to vary widely. Therefore, we attempted to improve the prediction accuracy by selecting multiple atmospheric stabilities covering the entire annual frequency of occurrence, and also added two cases of wind directions at ±11 degrees from both ends of the wind direction sector N. In addition to N, the NNE, S, SSW, NW, and NNW wind direction sectors were selected, in order to validate the accuracy.

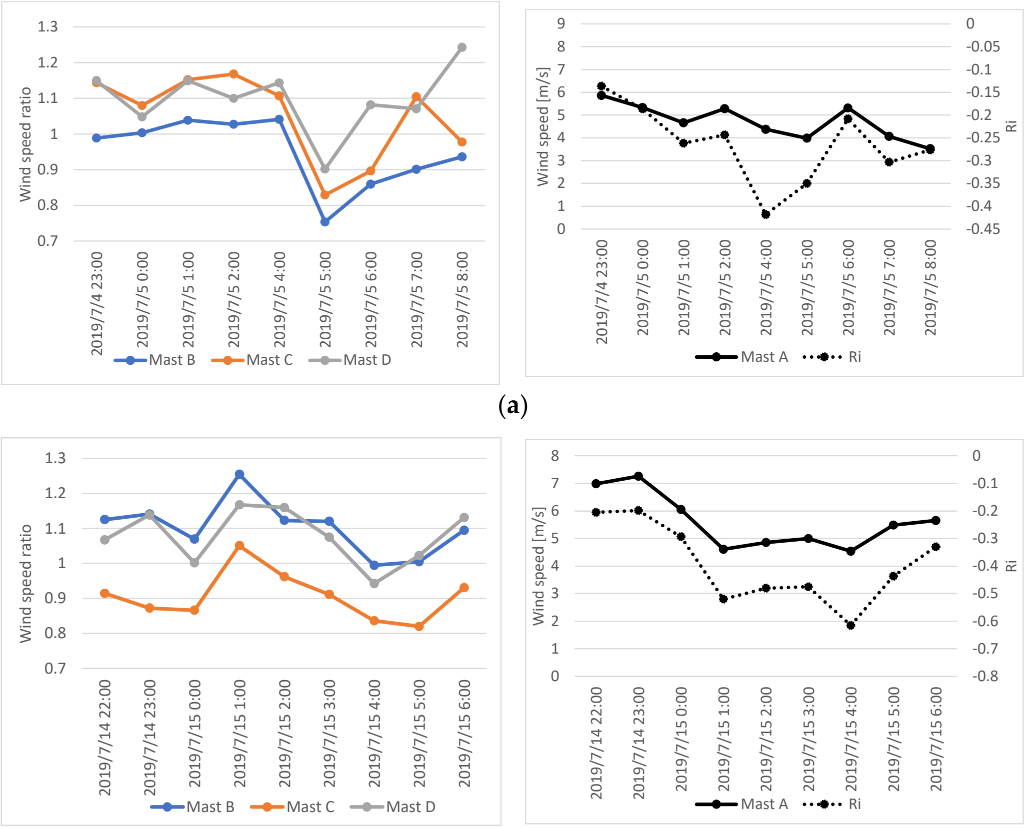

(**a**)

(**b**)

Figure 8. Time-series of the wind speed ratios and atmospheric stability: (**a**) From 23:00 on 4 July to 8:00 on 5 July 2019; and (**b**) from 22:00 on 14 July to 6:00 on 15 July 2019.

3.4. Decision of Atmospheric Stability for Numerical Simulation

To ensure that the airflow simulation covered the entire frequency of occurrence of atmospheric stability, the frequency of occurrence was assessed for each wind direction and multiple atmospheric stability conditions were selected. Figure 9 shows the frequency distributions of atmospheric stability for the six wind direction sectors subjected to airflow simulations.

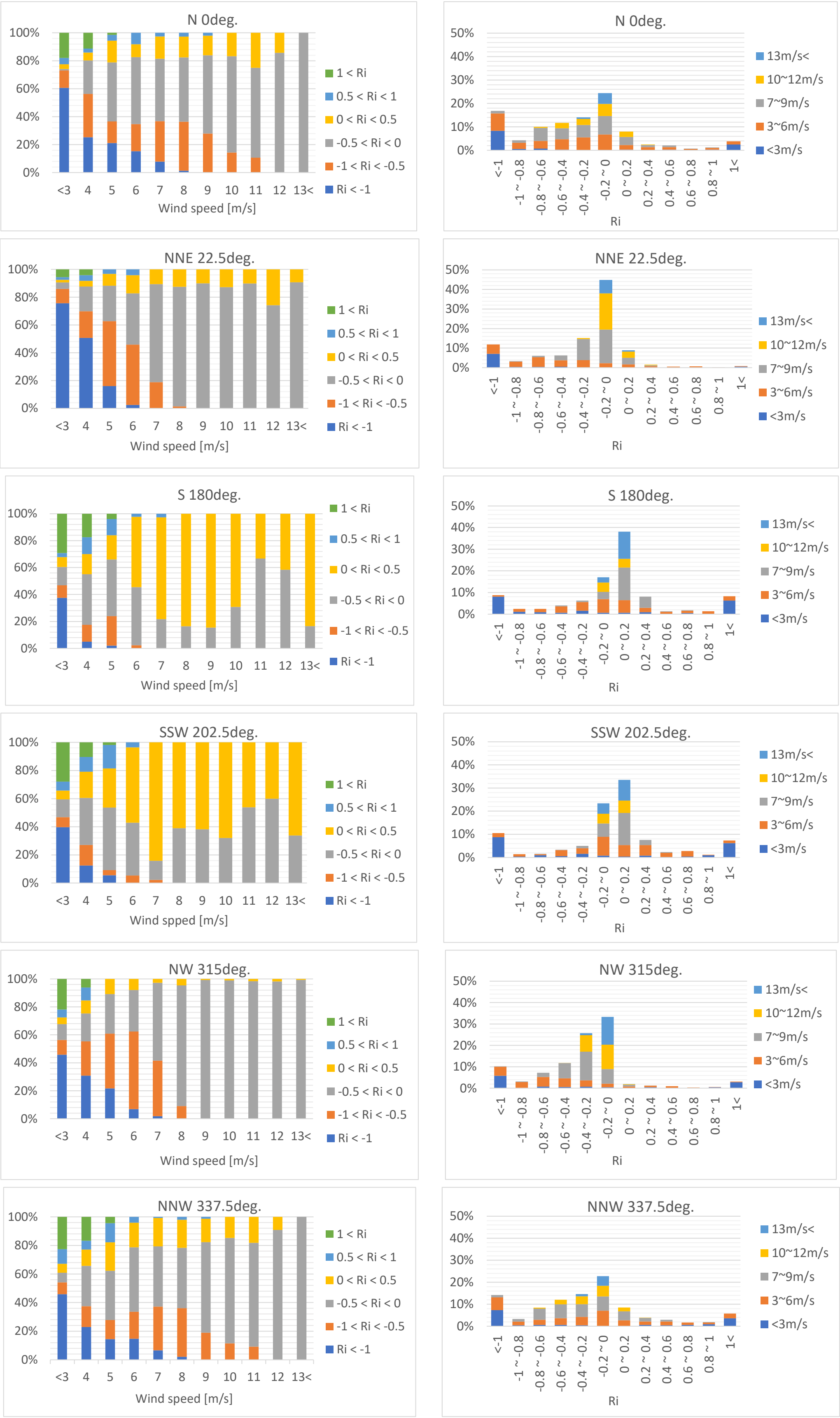

Figure 9. Appearance frequencies of atmospheric stability in the six selected wind direction sectors.

A wide range of Ri values were observed for each wind direction sector, suggesting that a variety of atmospheric stabilities other than neutral were present. In the N, NNE, and NNW directions, Ri distribution was biased toward the unstable side, but stable conditions up to about Ri = +0.2 also occurred. Similarly, in the NW direction, the Ri distribution was biased toward the unstable side, but stable conditions rarely occurred. In the S and SSW direction, Ri roughly occurred in the range of −0.2 to +0.2 (i.e., from unstable to stable conditions), centered on neutral. The sea surface temperature is relatively high in this region, due to the warm current. In autumn, winter, and spring, NW to NNE wind directions occur more frequently, and the temperature is lower than the sea surface temperature, resulting in more unstable conditions. S and SSW winds occur more frequently in summer, and the atmospheric stability tends to be close to a neutral condition, as the temperature increases and becomes similar to the sea surface temperature. The frequency of atmospheric stability differed for each wind direction. Thus, to cover the whole situation, airflow simulations were performed for each wind direction with the atmospheric stabilities shown in Table 1.

Table 1. Analysis case for atmospheric stability and wind direction.

	N	**NNE**	**S**	**SSW**	**NW**	**NNW**
Ri = −0.5	√	√	-	-	√	√
Ri = −0.2	√	√	√	√	√	√
Ri = 0	√	√	√	√	√	√
Ri = +0.2	√	√	√	√	-	√

4. Numerical Simulation

4.1. Summary of the Numerical Simulation Methods

RIAM-COMPACT, a commercial numerical simulation software that can perform unsteady non-linear analysis using LES, was used to simulate the separation and eddies caused by topographic undulations. The method is based on the finite difference method. Details of the numerical simulation method used by RIAM-COMPACT can be found in [3,9,13–16]. The governing equations used in this study are shown in [3] (p. 10). As an example of the computational domain and boundary conditions, the case for the north wind is shown in Figure 10. The analysis area was 7.0 (x) km in the mainstream direction, 4.5 (y) km in the mainstream perpendicular direction, and 1.4 (z) km in the vertical direction, using 2 m numerical elevation data acquired in an aerial laser survey. The highest elevation on Enoshima Island is 140 m and it is denoted by h. Based on the height of h, the computational domain was set 25 h upstream and downstream directions from the analysis center for the mainstream direction, 16 h from the center to both sides for the perpendicular to the mainstream direction, and 10 h for the vertical direction. In this study, the horizontal grid was equally spaced at 25 m and unequally spaced to be coarser near the outflow boundary. The effect of horizontal mesh size is shown in Appendix A. The grid in the vertical direction was unequally spaced, becoming finer at the ground surface, with a minimum spacing of approximately 1 m. The airflow is easily separated from the ground surface due to its undulation, and the vertical wind speed profile is strongly influenced by the ground surface, which will be shown in Section 4.2.1, but the profile was considered resolvable with a minimum vertical grid size of 1 m. For the grid resolution in a terrain such as at this site, it has been shown by Uchida et al. [3,15], that airflow separation due to terrain can be reproduced using these settings. The number of grid points was 241 (x) × 181 (y) × 41 (z), or about 1.7 million. The inflow was a constant wind with a 0.1 vertical shear profile. To generate inflow wind variability, a block was set at the position shown in Figure 10, at one-tenth the height of the maximum elevation difference. A free-slip boundary condition was applied to the side and upper walls, a convective outflow condition was applied to the outlet boundary, and a no-slip condition was imposed on the ground surface. These boundary conditions are shown in Figure 10. The time step was $\Delta t = 2 \times 10^{-3}$ h/U. Here, h is the maximum terrain elevation within the computational domain; U is the wind speed at the inflow boundary at the height of the maximum terrain elevation within the computational domain. It has been shown by Uchida et al. [21] for a complex terrain site such as this site, that airflow separation due to terrain can be reproduced using $\Delta t = 2 \times 10^{-3}$ h/U.

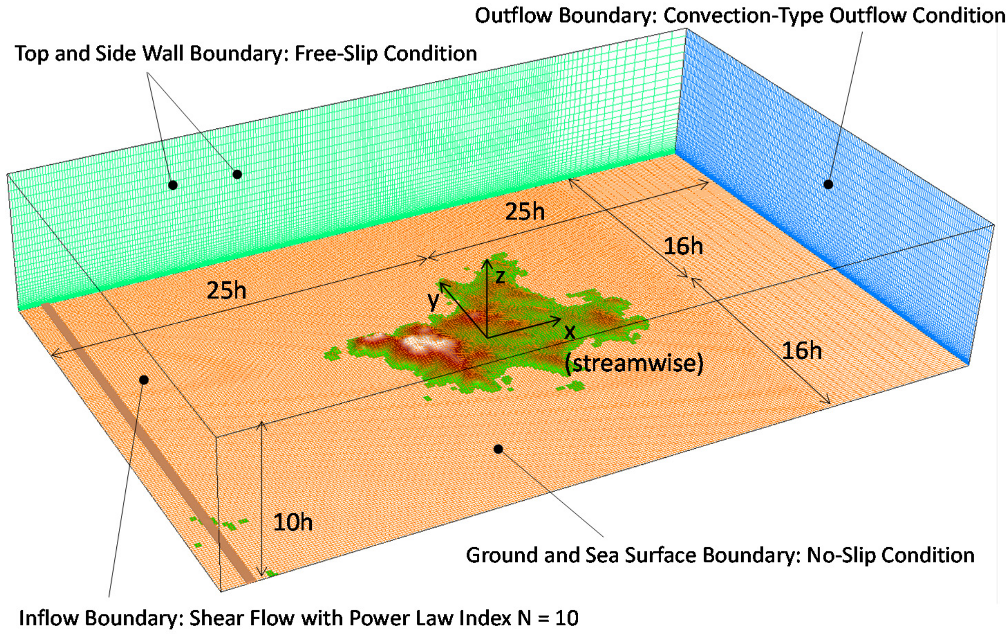

Figure 10. Computational domain.

4.2. Results and Discussions

4.2.1. Validation of Vertical Profile

Figure 11 shows the results for the vertical distribution of wind speed at each mast in the N, S and NW wind direction sectors, representing the six wind directions for which the analysis was run. The measured heights of the masts were 58, 50, and 40 m, respectively, and the figures are expressed as a ratio compared to the wind speed at 58 m altitude. The measurements showed different vertical profiles, depending on the mast position and wind direction, indicating that separation and wind speed acceleration due to topography could occur. The vertical profile results of the airflow simulations reproduced the trends of the actual measurements, although the differences in atmospheric stability varied. The wind speed at 40 m altitude was significantly lower at mast A in the wind direction sector N, which was caused by air flow separation, presumably because mast A is located at a slightly lower altitude on the downwind side from the top of the mountain, as shown in the topographic map in Figure 3. The vertical profiles of wind speed ratio calculated by the airflow simulation varied, depending on the atmospheric stability, and did not agree with the measurements when the atmospheric stability was neutral (Ri = 0), which is used in the conventional method. Furthermore, the measurements included variations caused by atmospheric stability. We inferred that the measured vertical profile included various vertical profiles caused by various atmospheric stability levels.

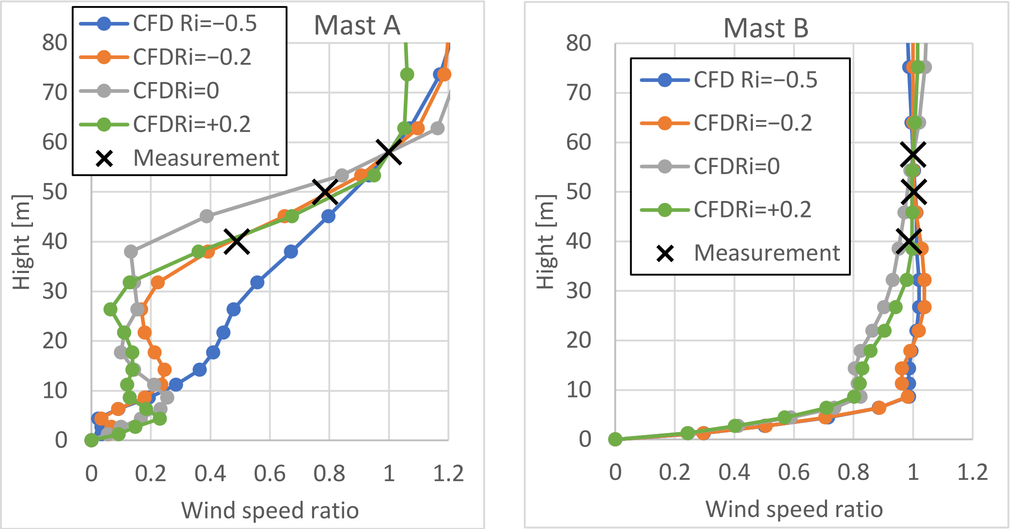

Wind direction N Wind direction N

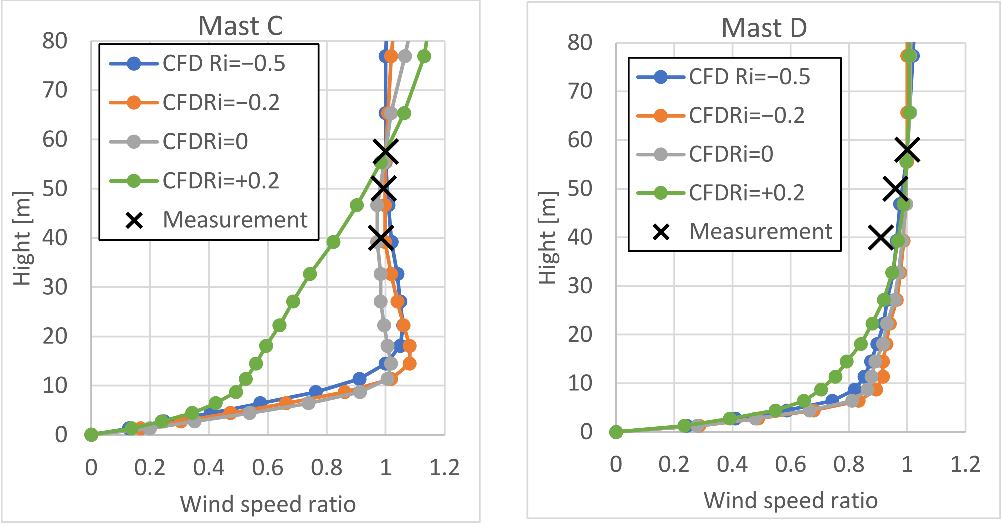

Wind direction N Wind direction N

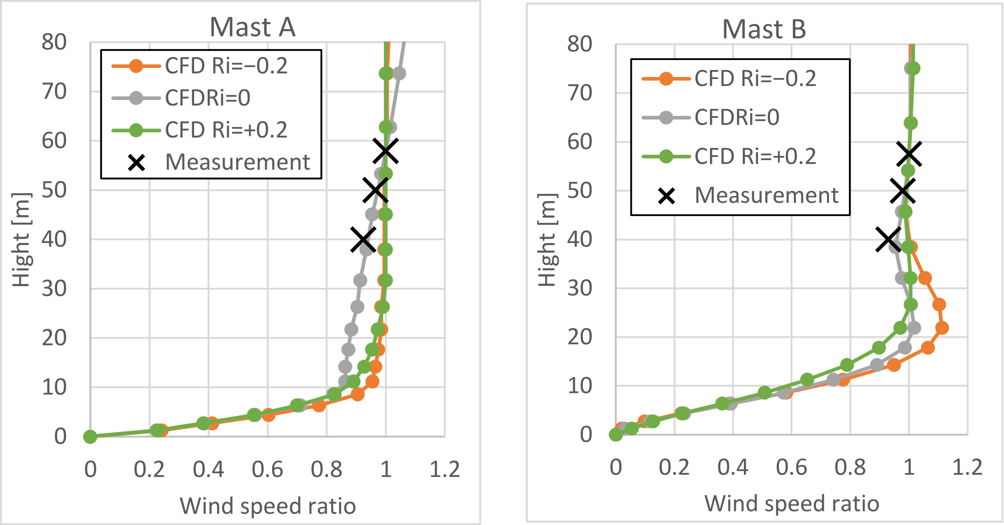

Wind direction S Wind direction S

Figure 11. *Cont.*

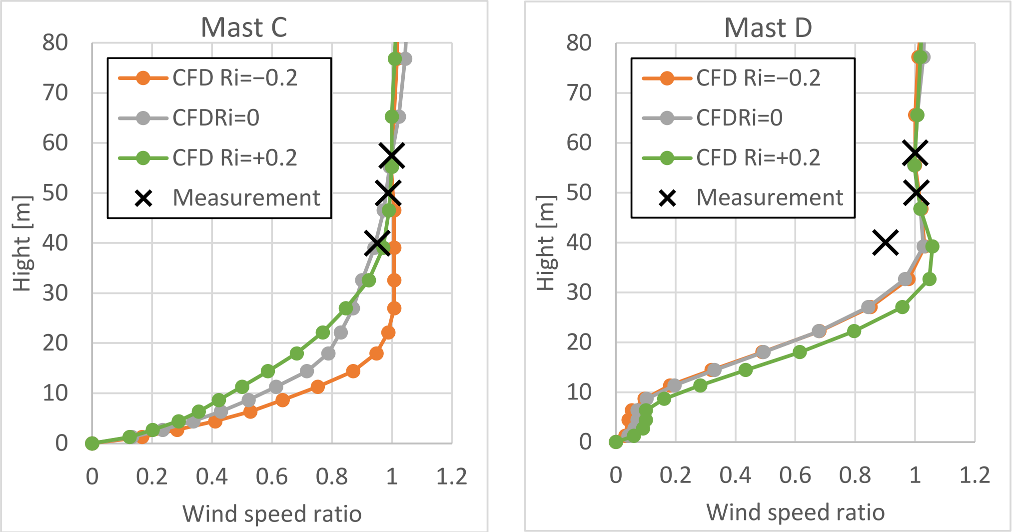

Wind direction S Wind direction S

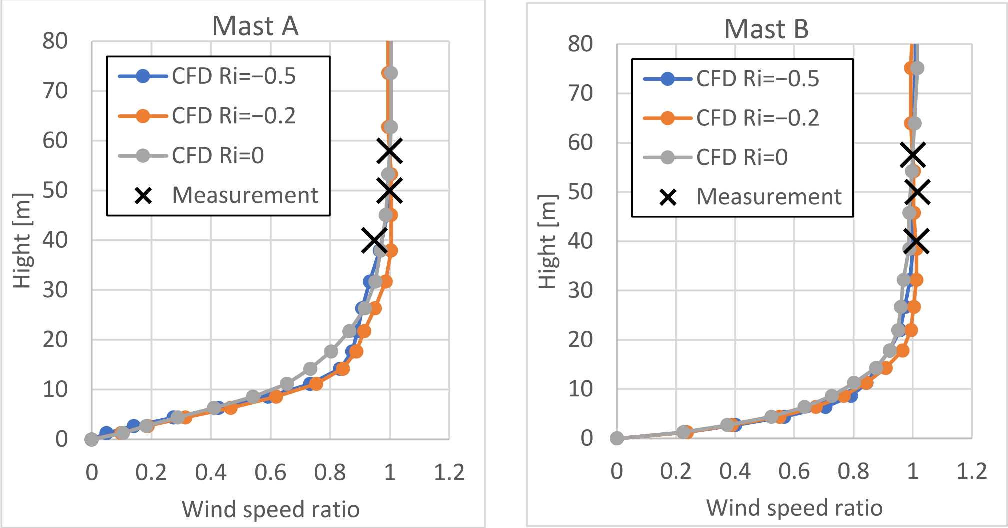

Wind direction NW Wind direction NW

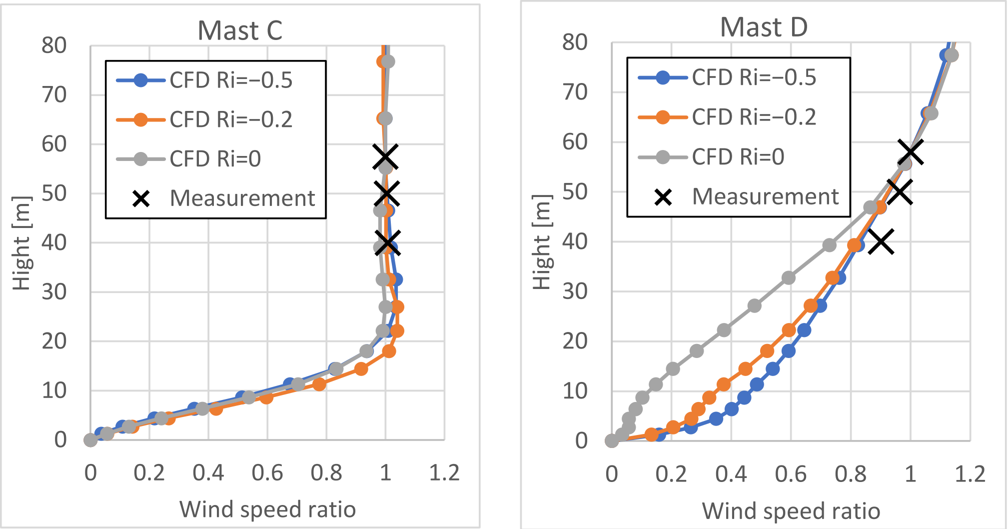

Wind direction NW Wind direction NW

Figure 11. Vertical wind speed profiles.

4.2.2. Validation of Wind Speed Ratio

For the wind speed ratios of masts B, C and D relative to mast A in the wind direction sector N, the airflow simulations were compared with the measurements. Figure 12 shows the wind speed ratios for 12 cases of air flow simulations, considering four cases of atmospheric stability and three wind directions. As the 16 wind divisions each had a width of 22 degrees, we broke down the three wind direction cases as the center of wind direction sector N, along with the wind directions shifted ±11 degrees from the center. The wind speed ratios changed significantly with atmospheric stability. When the wind direction was shifted by ±11 degrees, the change was small for mast B and relatively large for Masts C and D. Masts A and B are located at the north end of Enoshima Island, close to where the north wind flows in from the sea; thus, the changes in windward topography due to changes in wind direction are small at these masts. However, Mast C is located about 1 km from the north end of Enoshima Island and Mast D is located 1.8 km from the north end of Enoshima Island; thus, the changes in windward topography due to changes in wind direction are large. The change observed in the wind speed ratio due to the ±11-degree change in wind direction was presumably related to the large change in the upwind topography caused by the change in wind direction.

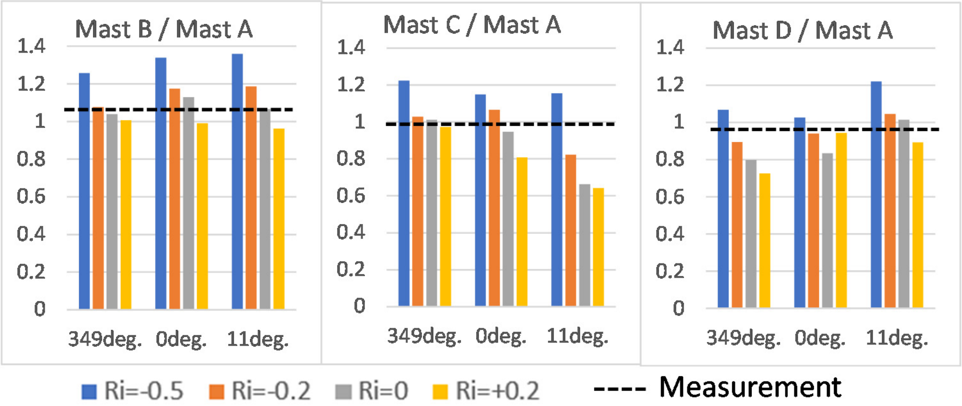

Figure 12. Comparison of the wind speed ratios in the wind direction sector N.

As mentioned in Section 3, even for the wind direction sector N, there was large variation in the measured mast-to-mast 1-h wind speed ratios. To take into account the various wind conditions, Four methods, listed in Table 2 were considered for verification of the simulation accuracy. When averaging the four atmospheric stability cases, a simple average was used, while the average of the three wind directions was taken as a weighted average based on the frequency of occurrence of the observed data within a sector width of 22.5 degrees. Specifically, the 22.5 deg. width was divided into four parts, and the proportion of the middle two (11.25 deg. width) was applied for analysis of the central wind direction of the sector; the proportion of the right side (5.125 deg. width) toward the windward direction was applied for the analysis at +11 deg.; and the proportion of the left side (5.125 deg. width) toward the windward direction was applied for the analysis at −11 deg.

Table 2. Composition of each method for wind direction sector N.

	Atmospheric Stability	**Inflow Wind Direction**
Method A	Neutral	Center (0 deg.)
Method B	Simple average (Ri = −0.5, −0.2, 0, +0.2)	Center (0 deg.)
Method C	Neutral	Weighted average (0 deg., 11 deg., 349 deg.)
Method D	Simple average (Ri = −0.5, −0.2, 0, +0.2)	Weighted average (0 deg., 11 deg., 349 deg.)

The wind speed ratios for Methods A and B are shown in Figure 13. The wind speed ratios of Mast B and Mast C with respect to Mast A were generally reproduced using the conventional method, with a neutral Ri of 0 and wind direction of 0 deg. (i.e., Method A), but there was a large error for Mast D. Method B was in good agreement with the measurement. The wind speed ratios of the simulations varied greatly, depending on the atmospheric stability, and the accuracy of the simulation was greatly improved by averaging these ratios. For Masts B and C, the wind speed ratio increased as the atmospheric stability moved from a stable, to neutral, to unstable condition. Mast D had the lowest wind speed ratio when it was neutral, and the wind speed ratio increased under both unstable and stable conditions.

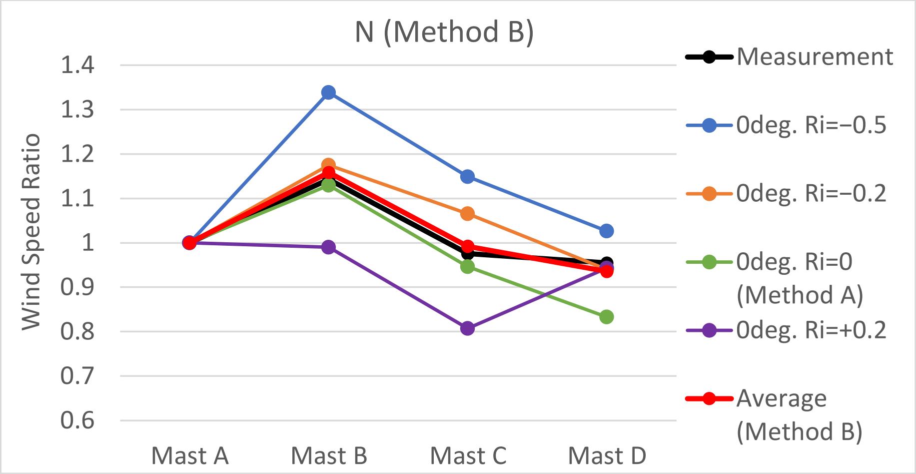

Figure 13. Wind speed ratios with respect to Mast A using Method B.

As the atmospheric stability becomes more stable, the airflow separation due to topography tends to subside. Additionally, neutral and unstable airflows are very complex, as they are easily separated. Under an unstable condition, the atmosphere is more likely to mix than under a neutral condition, making it easier to recover from a wind speed decrease in the separation region. However, easy mixing of the atmosphere also always produces turbulence. As a result, the effect of atmospheric stability on the wind speed ratio varied with location. The changes in airflow patterns due to atmospheric stability are explained in Section 4.2.3. The wind speed ratio for Method C is shown in Figure 14. Although the atmospheric stability was only neutral, it can be seen that the results of the wind speed ratio were very different when the wind direction was shifted by ±11 degrees. Even with the weighted averages, the accuracy did not improve, compared to the conventional method (i.e., Method A), which was set only with 0 degrees of wind direction and neutral atmospheric stability (Ri = 0). The results of Method D are shown in Figure 15. The color indicates the atmospheric stability, and the line style indicates the wind direction. Although the results of all 12 cases were very different, due to the simple average of the atmospheric stability and the weighted average of the wind direction based on the frequency of occurrence, Method D could reproduce the actual measurements with high accuracy.

The wind speed ratio results from the four methods are summarized in Figure 16, and their prediction errors are given in Table 3. Compared to Methods A and C, Methods B and D showed improvements, especially for Mast D. Mast D is subject to airflow that separates near Mast A and traverses the island. This position is difficult to predict, as it is located far from Mast A and is strongly affected by changes in airflow separation due to atmospheric stability. Method B, which was considered as an average of four cases of atmospheric stability with only one case of wind direction at the center, was sufficiently accurate; however, Method D, which represents an average of all cases, predicted the results at all three Masts with high accuracy (i.e., within 1.5% absolute error).

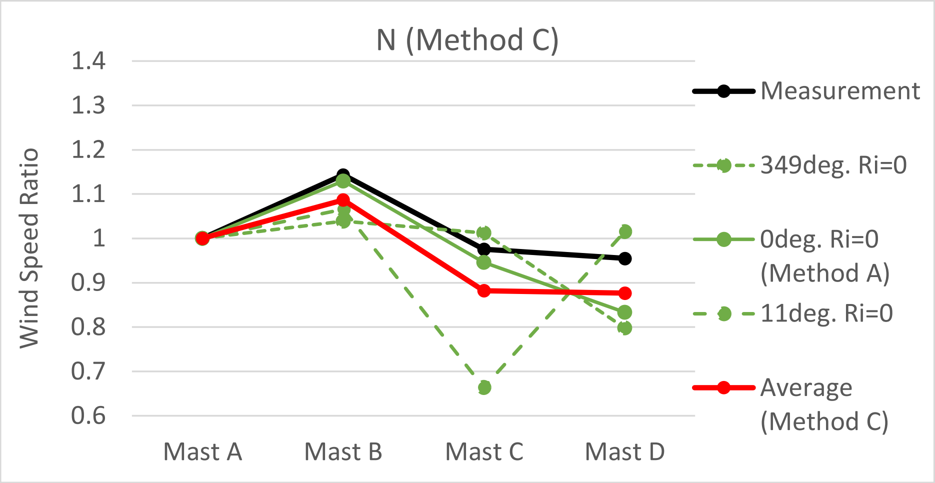

Figure 14. Wind speed ratios with respect to Mast A using Method C.

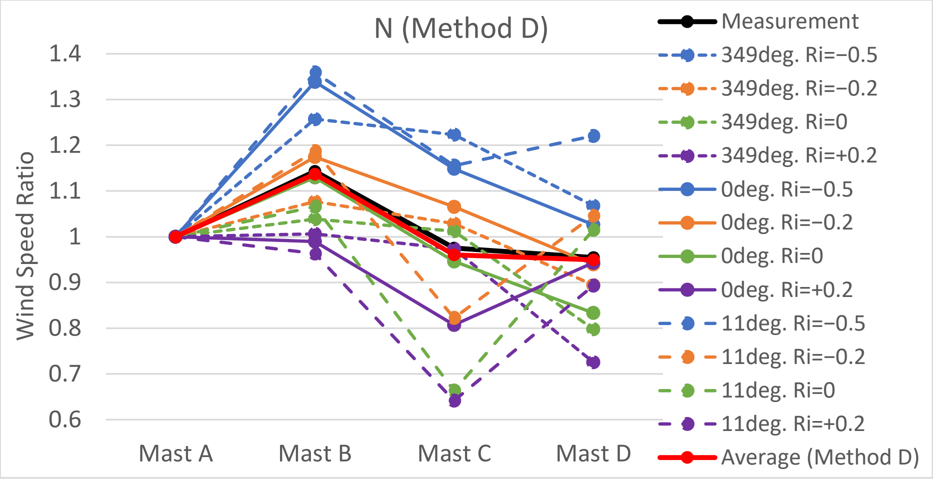

Figure 15. Wind speed ratios with respect to Mast A using Method D. The color indicates the atmospheric stability, while the line style indicates the wind direction.

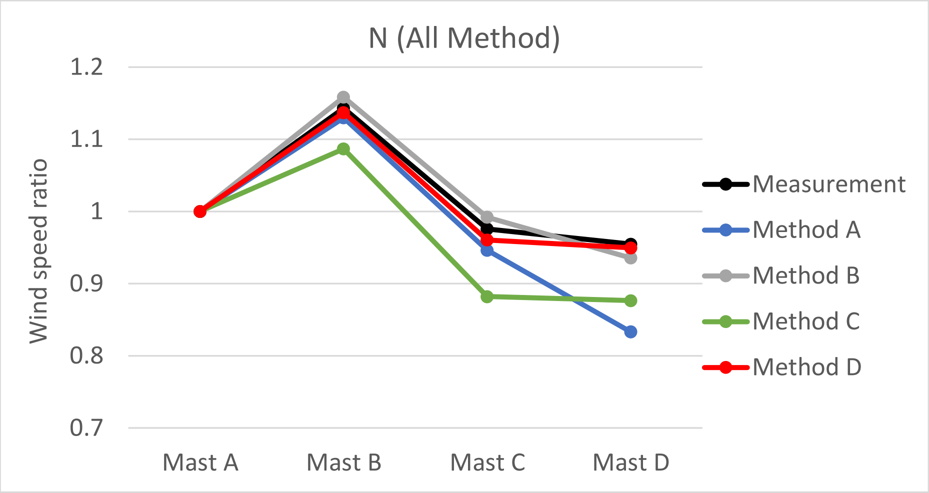

Figure 16. Comparison of wind speed ratios using all methods.

Table 3. Summary of prediction error for wind direction sector N.

	Method A	Method B	Method C	Method D
Error of Mast B	−1.2%	1.3%	−4.9%	−0.5%
Error of Mast C	−3.0%	1.7%	−9.6%	−1.5%
Error of Mast D	−12.7%	−2.0%	−8.2%	−0.5%
Averaged absolute error	5.6%	1.7%	7.6%	0.9%
Max of absolute error	12.7%	2.0%	9.6%	1.5%

For the wind direction sector N, Method D was able to predict the wind speed ratios with very high accuracy. To see how well this method works in other wind direction sectors, airflow simulations were also performed for the NNE, NNW, NW, SSW, and S wind directions. The atmospheric stability was set to the Ri values given in Table 1, and the wind direction was set to the center, +11 degrees, and −11 degrees in the wind direction sectors with width of 22.5 deg. The results for Method D, which used the results of the airflow simulations for all cases, are shown in Figure 17. The colors represent the atmospheric stabilities, and the line styles represent wind directions. The wind speed ratios from the airflow simulations changed, with different stability values in the same wind direction and, likewise, with different wind directions under the same stability values. This result indicates that the airflow is affected by the atmospheric stability conditions and the wind directions within 11 degrees. The measured wind speed ratios were generally within the variability of each case and, as a result, Method D was able to reproduce the measured trends and reduce the risk of large prediction errors.

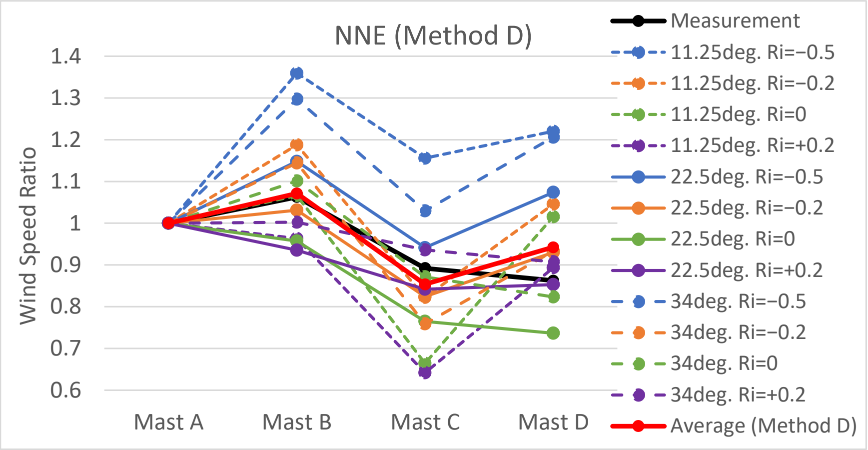

(**a**)

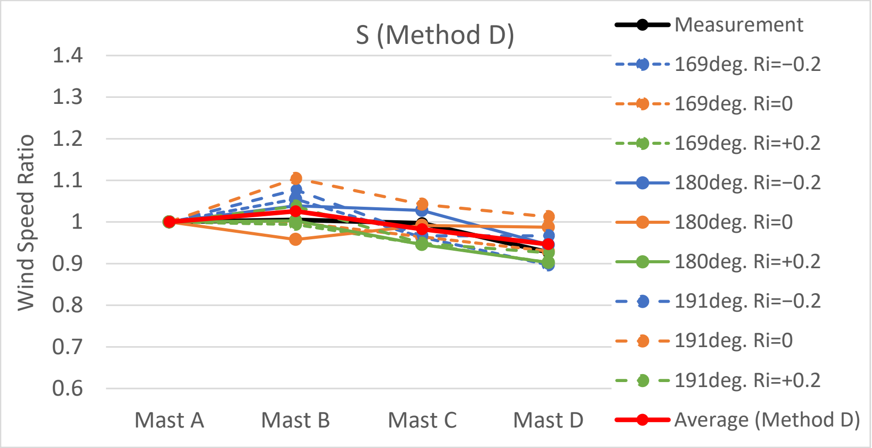

(**b**)

Figure 17. *Cont.*

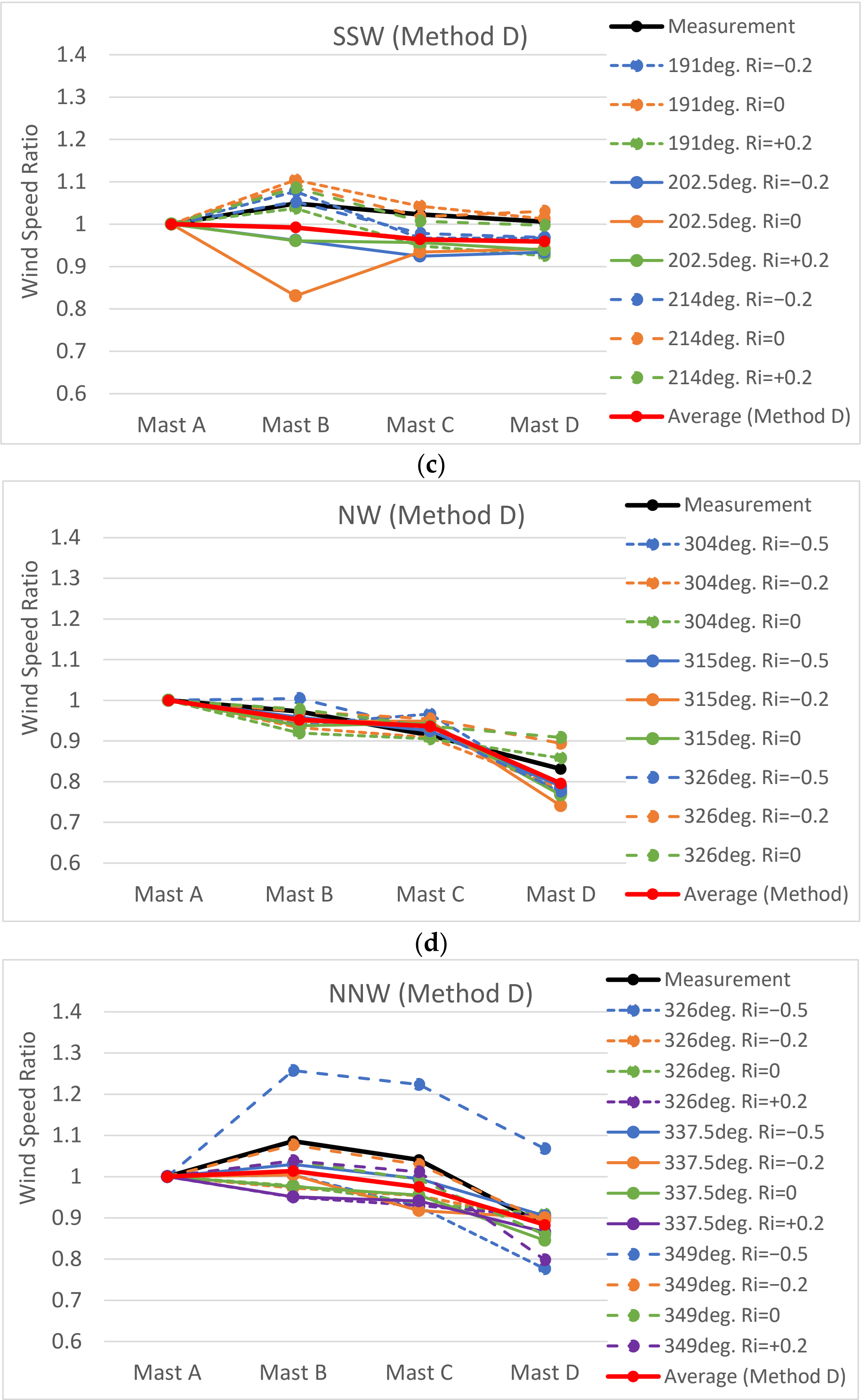

(**c**)

(**d**)

(**e**)

Figure 17. Comparison of wind speed ratios in various atmospheric stabilities and wind directions using method D. The color indicates the atmospheric stability, while the line style indicates the wind direction. (**a**) Wind direction NNE; (**b**) Wind direction S; (**c**) Wind direction SSW; (**d**) Wind direction NW; (**e**) Wind direction NNW.

Figure 18 shows the results of each method for each wind direction sector. Method D, which took the average of all the cases, featured no large errors and showed a trend that was relatively consistent with the actual measurements in all wind direction sectors.

Figure 19 shows the mean absolute error and the maximum absolute error for each mast in each wind direction, from which it can be seen that Method D was the best method, with demonstrably small errors. On the other hand, the conventional method (i.e., Method A) had the lowest accuracy.

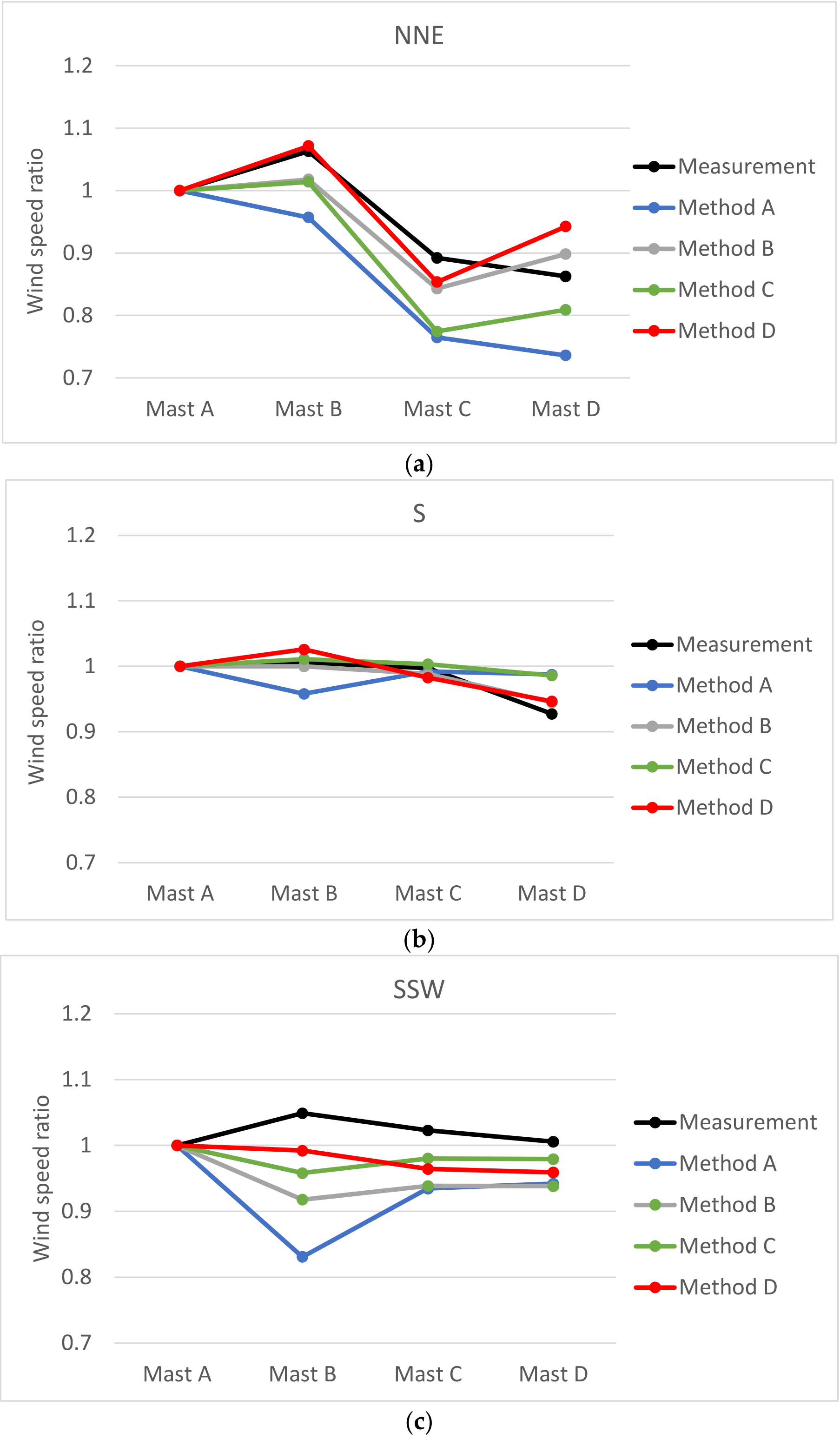

Figure 18. *Cont*.

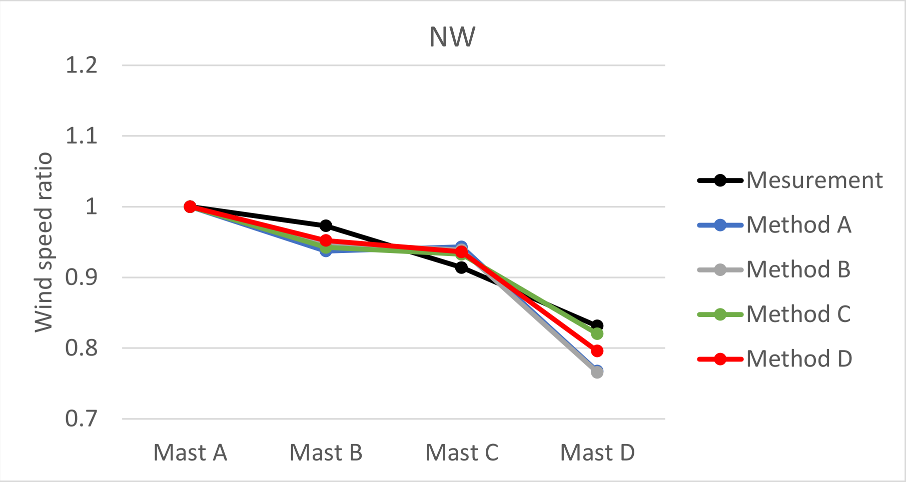

(**d**)

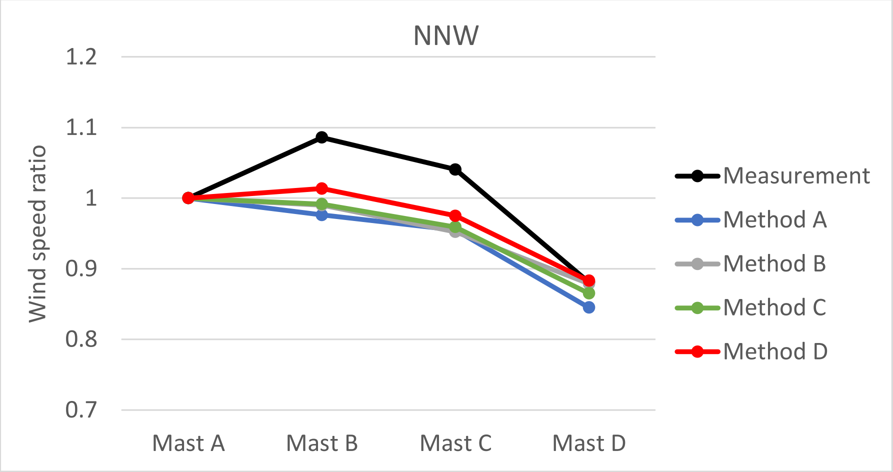

(**e**)

Figure 18. Comparison of wind speed ratios with all methods for wind direction sectors NNE, S, SSW, NW, and NNW. (**a**) Wind direction NNE; (**b**) Wind direction S; (**c**) Wind direction SSW; (**d**) Wind direction NW; (**e**) Wind direction NNW.

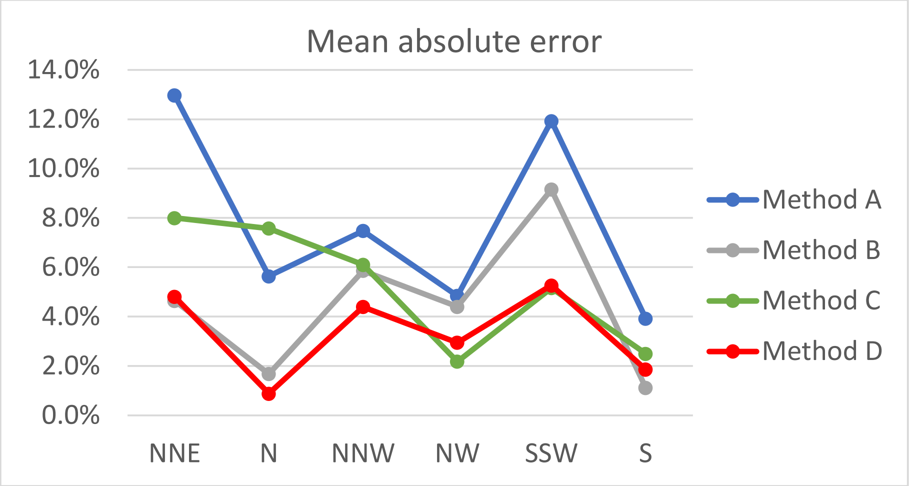

(**a**)

Figure 19. *Cont.*

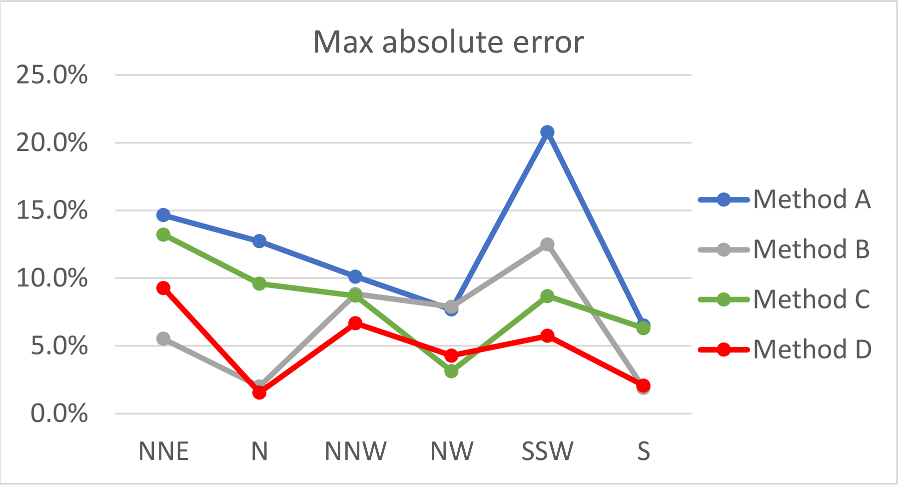

(**b**)

Figure 19. Comparison of prediction errors of all methods for various wind direction sectors. (**a**) Mean absolute error; (**b**) Maximum absolute error.

Table 4 shows the mean absolute error for all wind direction sectors (average in Figure 19a), the mean of the maximum absolute error for each wind direction sector (average in Figure 19b), and the maximum absolute error for all wind direction sectors (maximum in Figure 19b) for each method. Overall, Method D was the best, with less than half of the error obtained by the conventional method (Method A). The mean absolute error was 3.4%, the mean maximum error for each wind direction was less than 5%, and the maximum error in all cases was less than 10%, indicating that Method D can predict the wind conditions with high accuracy. Although Method B was applied only to the central wind direction, by incorporating multiple atmospheric stabilities, it obtained the second-best result. The results of this method were relatively good, even though the number of analysis cases was one-third that of Method D.

Table 4. Summary of prediction error for all methods.

Method	A	B	C	D
Mean absolute error	7.8%	4.5%	5.3%	3.4%
Mean of the maximum absolute error for each wind direction sector	12.1%	6.4%	8.3%	4.9%
Maximum absolute error	20.8%	12.5%	13.2%	9.3%

4.2.3. Wind Speed Distribution in a Numerical Simulation

We confirmed how the airflow through Enoshima Island changes, depending on the atmospheric stability, through visualization using a simulation. Figure 20 shows the simulated wind speed distributions in the north wind for an unstable atmosphere (Ri = −0.5), a neutral atmosphere (Ri = 0), and a stable atmosphere (Ri = +0.2), showing slices of an instant in the unsteady calculations. As the atmospheric stability was unstable, turbulence began to form over the sea surface before reaching Enoshima. After separation by the terrain, mixing of the separated region and the upper flow could be observed. In the neutral case, after separation by the terrain, mixing between the separation region and the upper flow did not proceed very far, indicating that the separation area remained distant. In the stable case, separation occurred at the terrain, but quickly re-attached to the ground surface on the leeward side, resulting in a small separation region. Under this northerly wind, Mast D was located just downwind of Mast A. As shown in Figure 13, the wind speed at Mast D was almost 20% lower than that at Mast A under neutral conditions; however, when the conditions became stable or unstable, the wind speed became equal to that at

Mast A. Under stable conditions, the separation region was small while, in the unstable condition, mixing proceeded in the upper and lower layers. As a result, Masts A and D showed the same wind speed. Under neutral conditions, Mast D entered the separation region and, thus, showed a lower wind speed than Mast A.

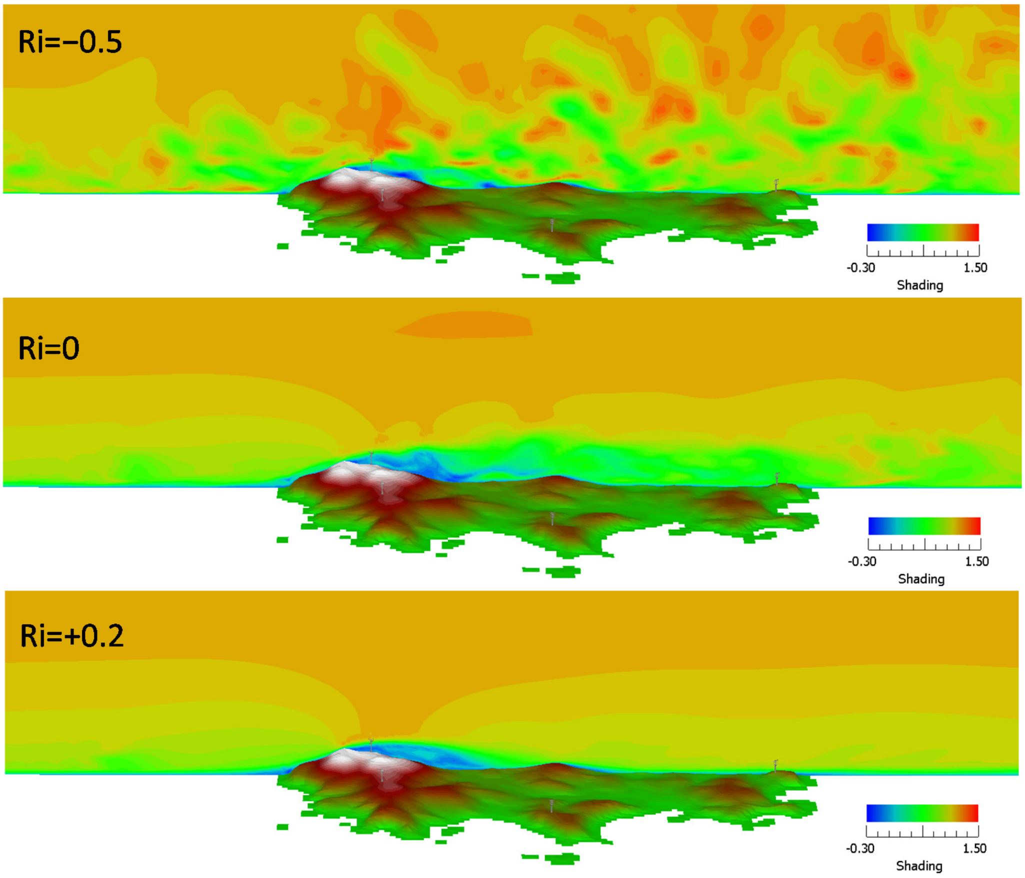

Figure 20. Simulated wind speed distributions for unstable (Ri = −0.5), neutral (Ri = 0), and stable (Ri = +0.2) atmospheric stability scenarios in the north wind. These are slices of an instant in the unsteady calculation. The shading color bar represents the dimensionless wind speed with respect to the inflow streamwise wind speed at the height of the maximum surface elevation in the computational domain.

Figure 21 shows the wind speed distribution around Masts A and B. The left mast is Mast A, while Mast B is to the right. Mast A was located at a slightly lower elevation than the top of the windward mountain, and the airflow was separated at the top in front of Mast A. As shown in Figure 21a, on the windward side of Mast A's position, turbulence had already occurred before the airflow entered the island in the unsteady condition. In the neutral condition, the smooth airflow separated at the top of the mountain, and the separation region appeared stronger in the neutral condition than that in the unstable condition. Therefore, as shown by the north wind in Figure 11, the vertical profile of the neutral condition had a stronger separation at lower altitudes. This phenomenon can be seen in Figure 21b. As shown in Figure 21b (left), the unsteady condition at Mast B led to a high wind speed, even at a low altitude, due to mixing of the upper and lower layers, as shown in Figure 21a (left). As a result, the acceleration effect due to the terrain was higher than that in the neutral condition. This effect can be observed in Figure 13, which shows that Mast B had a higher wind speed than Mast A under the unsteady condition of Ri = −0.5.

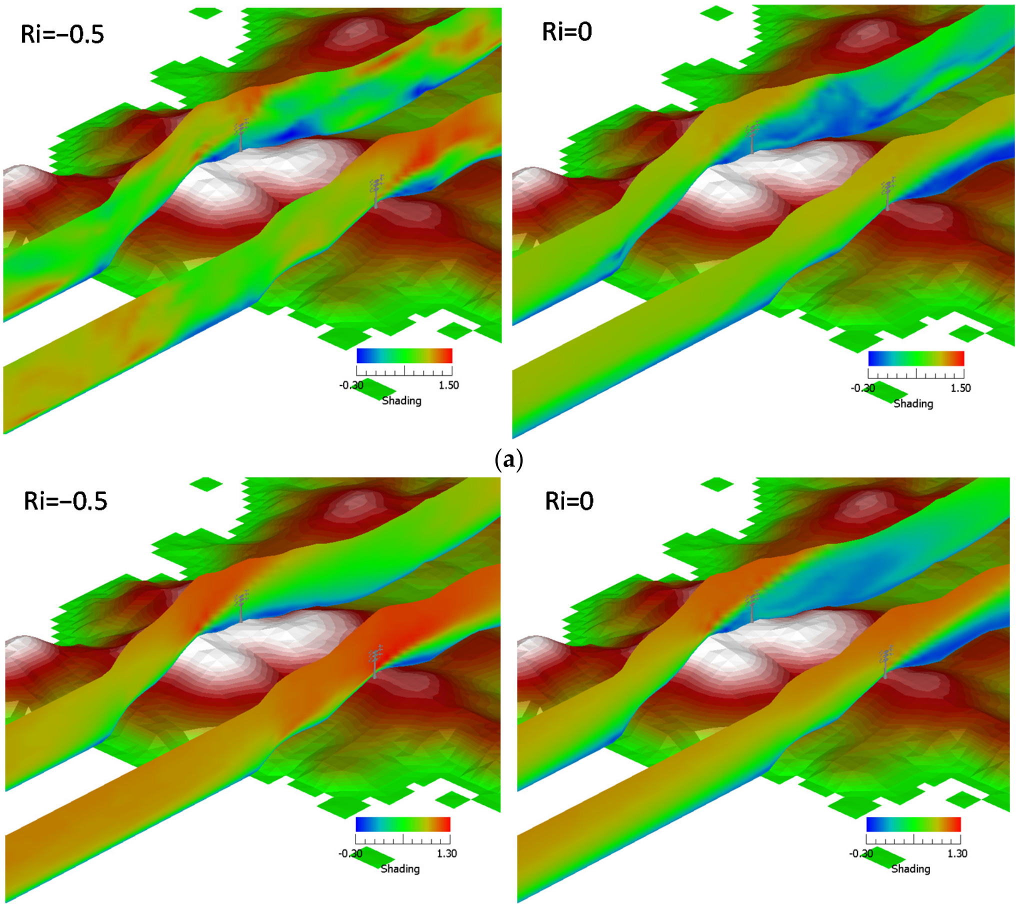

(**a**)

(**b**)

Figure 21. Simulated wind speed distributions for unstable atmospheric stability (Ri = −0.5) and neutral atmospheric stability (Ri = 0) in the north wind. Enlarged view around Masts A and B. The shaded color bar represents the dimensionless wind speed with respect to the inflow streamwise wind speed at the height of the maximum surface elevation in the computational domain. (**a**) Slices of an instant in the unsteady calculation; (**b**) Average wind speed distribution.

5. Conclusions

The main purpose of this study was to improve airflow simulations for wind resource assessments of onshore and offshore wind farms affected by topography. Due to the complex topography of the island that represents the subject of this study, the wind speed varied greatly with the mast position, even when focusing on a specific wind direction. In the conventional method, the analytical wind direction is divided into 12 or 16 parts, an airflow simulation is performed assuming neutral atmospheric stability, and one wind speed ratio is calculated for each wind direction. However, even when limited to a specific wind direction, the variation in the measured mast-to-mast wind speed ratio was large, suggesting the existence of a variety of airflows. The atmospheric stability calculated from the ERA5 sea surface temperature and the temperature at the observation mast presented a wide range of results, including stable, neutral, and unstable conditions. It is clear that the conventional method, which assumes only neutral atmospheric stability, does not correspond to the reality of various meteorological conditions. On the other hand, the atmospheric stability defined in this study alone was not enough to clarify the cause of the variation in the measured wind speed ratios. In reality, there are many varieties of winds that cannot be classified using only 16 wind direction categories and the atmospheric stability defined by Equation (1). In this study, the atmospheric stability was set based on the temperature difference between the air temperature and the sea surface temperature of the airflow, which was assumed to be uniform in the vertical direction. In reality, however, various temperature distributions occurred in the vertical direction. Moreover, the influence of terrain was not uniform within the 22.5-degree widths of the 16 wind direction sectors. However, it is unrealistic to calculate all possible situations when predicting annual energy production in a wind power feasibility assessment. Therefore, we sought to improve the prediction accuracy by selecting several atmospheric stabilities, in order to cover the entire annual frequency of occurrence and added the cases of ±11 degrees at both ends of the 16 wind direction sectors, in addition to the central wind direction. As a result, both the mean and maximum errors were reduced to half of that when using the conventional method. Since the accuracy of the annual energy production as well as wind speed is important in wind resource assessment [3], we plan to examine this point soon.

In this study, the results of three wind direction cases (center and ±11 degrees) were presented as a weighted average with respect to their frequency of occurrence; however, for atmospheric stability, we used a simple average over the multiple cases selected. For atmospheric stability, further improvements to the prediction accuracy could be considered by selecting appropriate Ri values or weighted averaging corresponding to the frequency of occurrence. Furthermore, optimization of the number of analysis cases will be considered in future work. For annual wind prediction, this method requires a very large number of LES analysis cases: more than 100 cases are needed to calculate the atmospheric stability of three to four cases for 32 wind directions. As it is not practical to continue using this method as-is, we will consider both reducing the computational load and improving the prediction accuracy by identifying the typical atmospheric stability and narrowing down the analysis cases. Nevertheless, while an increase in computational load relative to the conventional method is unavoidable, this increased load can be handled by a planned analysis schedule, as the installation of wind measurement masts for wind farm projects requires time for site land-use and permit surveys, and the measurement period after installation is typically greater than one year. After determining the best analysis method for this site, we will further evaluate the effectiveness of this method by increasing the number of sites to be validated.

Author Contributions: Project administration, Conceptualization, Software and Methodology, T.U.; Formal analysis and Validation, S.T. All authors prepared the manuscript. All authors have read and agreed to the published version of the manuscript.

Funding: This research received no external funding.

Institutional Review Board Statement: Not applicable.

Informed Consent Statement: Not applicable.

Data Availability Statement: Not applicable.

Acknowledgments: This study was supported by joint research between Kyusyu university and Japan Renewable Energy Corporation (principal investigator: Takanori Uchida). We would like to express our gratitude to the people concerned.

Conflicts of Interest: All authors declare no conflict of interest.

Nomenclature

Ri	Richardson number
U	streamwise wind speed [m/s]
x	streamwise coordinate [m]
y	streamwise perpendicular coordinate [m]
z	vertical coordinate [m]
θ_{bottom}	sea surface temperature [K]
θ_{in}	in flow temperature [K]

Appendix A Effect of Grid Resolution on Wind Speed Ratio

The effect of grid resolution on the wind speed ratio was examined. In this study, the horizontal grid resolution was set to 25 m. However, wind speed ratios were also calculated for horizontal grid sizes of 10 m, 15 m, 35 m, and 50 m in a north wind and under neutral atmospheric stability. The computational grids around Enoshima Island are shown in Figure A1, and the wind speed ratio results are shown in Figure A2. The change in the wind speed ratio for the grid size 25 m and over is large, but the change is small 25 m and under. There is a slight difference between grid sizes of 10 m and 25 m, but since the number of grids of 10 m grid size is more than six times larger than 25 m, grid size of 25 m was selected for both practicality and accuracy in the wind power business.

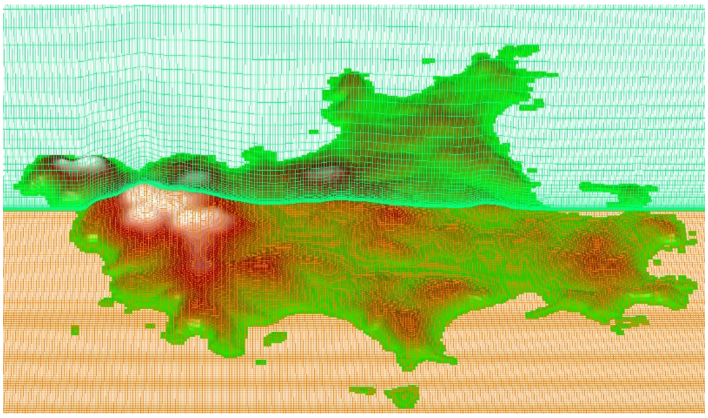

(**a**) 10 m

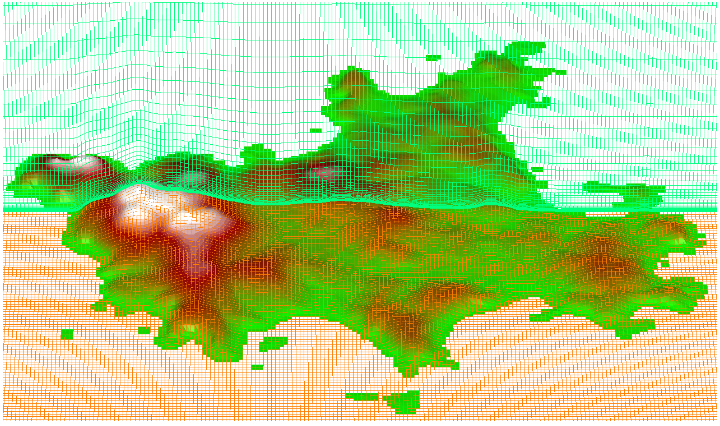

(**b**) 15 m

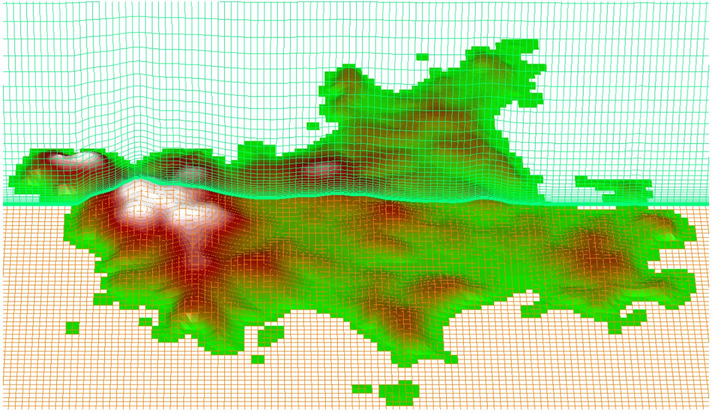

(**c**) 25 m

Figure A1. *Cont.*

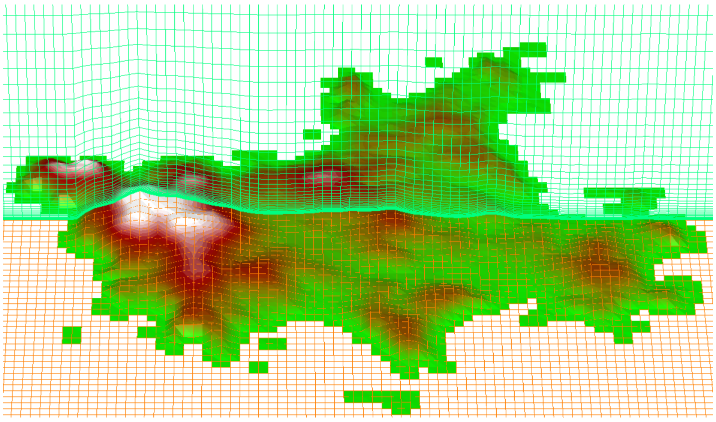

(**d**) 35 m

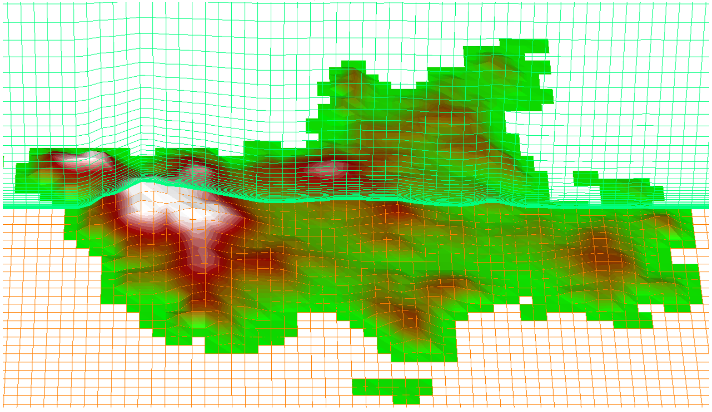

(**e**) 50 m

Figure A1. Comparison of computational grids around Enoshima Island. (**a**) Mesh size 10 m; (**b**) Mesh size 15 m; (**c**) Mesh size 25 m; (**d**) Mesh size 35 m; (**e**) Mesh size 50 m.

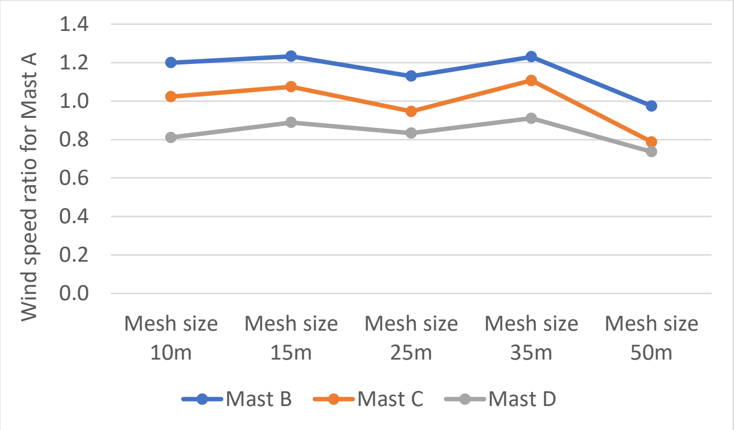

Figure A2. Variation of wind speed ratio for Mast A with mesh size.

References

1. Japan Wind Power Association Report. Available online: https://jwpa.jp/en/information/6105/ (accessed on 30 November 2018).
2. Stull, R.B. *An Introduction to Boundary Layer Meteorology*; Kluwer Academic Publishers: Dordrecht, The Netherlands, 1998.
3. Uchida, T.; Takakuwa, S. Numerical Investigation of Stable Stratification Effects on Wind Resource Assessment in Complex Terrain. *Energies* **2020**, *13*, 6638. [CrossRef]
4. Porté-Agel, F.; Bastankhah, M.; Shamsoddin, S. Wind-Turbine and Wind-Farm Flows: A Review. *Bound. Layer Meteorol.* **2020**, *174*, 1–59. [CrossRef] [PubMed]
5. Dörenkämper, M.; Witha, B.; Steinfeld, G.; Heinemann, D.; Kühn, M. The impact of stable atmospheric boundary layers on wind-turbine wakes within offshore wind farms. *J. Wind. Eng. Ind. Aerodyn.* **2015**, *144*, 146–153. [CrossRef]

6. Abkar, M.; Porté-Agel, F. The Effect of Free-Atmosphere Stratification on Boundary-Layer Flow and Power Output from Very Large Wind Farms. *Energies* **2013**, *6*, 2338–2361. [CrossRef]
7. Lu, H.; Porté-Agel, F. Large-eddy simulation of a very large wind farm in a stable atmospheric boundary layer. *Phys. Fluids* **2011**, *23*, 065101. [CrossRef]
8. Weather Research and Forecasting Model. Available online: https://www.mmm.ucar.edu/weather-research-and-forecasting-model (accessed on 2 December 2021).
9. Uchida, T.; Li, G. Comparison of RANS and LES in the Prediction of Airflow Field over Steep Complex Terrain. *Open J. Fluid Dyn.* **2018**, *8*, 286–307. [CrossRef]
10. FY2020 Promising Sea Areas and Sites Selected for Future Designation of Project Target Areas. Available online: https://www.meti.go.jp/english/press/2020/0703_003.html (accessed on 1 April 2021).
11. JRE and wpd to Conduct Joint Enterprise in Saikai Enoshima Offshore Wind Power Project. Available online: https://www.jre.co.jp/news/pdf/news_20210907_E.pdf (accessed on 7 September 2021).
12. ERA5. Available online: https://www.ecmwf.int/en/forecasts/datasets/reanalysis-datasets/era5 (accessed on 1 September 2020).
13. Uchida, T.; Ohya, Y. Micro-siting technique for wind turbine generators by using large-eddy simulation. *J. Wind. Eng. Ind. Aerodyn.* **2008**, *96*, 2121–2138. [CrossRef]
14. Uchida, T. Computational Fluid Dynamics Approach to Predict the Actual Wind Speed over Complex Terrain. *Energies* **2018**, *11*, 1694. [CrossRef]
15. Uchida, T.; Sugitani, K. Numerical and Experimental Study of Topographic Speed-Up Effects in Complex Terrain. *Energies* **2020**, *13*, 3896. [CrossRef]
16. Uchida, T.; Takakuwa, S. A Large-Eddy Simulation-Based Assessment of the Risk of Wind Turbine Failures Due to Terrain-Induced Turbulence over a Wind Farm in Complex Terrain. *Energies* **2019**, *12*, 1925. [CrossRef]
17. Rodrigo, J.S.; Gancarski, P.; Arroyo, R.B.; Moriarty, P.; Chuchfield, M.; Naughton, J.W.; Hansen, K.S.; Machefaux, E.; Koblitz, T.; Maguire, E.; et al. IEA-Task 31 WAKEBENCH: Towards a protocol for wind farm flow model evaluation. Part 1: Flow over-terrain models. *J. Phys. Conf. Ser.* **2014**, *524*, 012105. [CrossRef]
18. Moriarty, P.; Rodrigo, J.S.; Gancarski, P.; Chuchfield, M.; Naughton, J.W.; Hansen, K.S.; Machefaux, E.; Maguire, E.; Castellani, F.; Terzi, L.; et al. IEA-Task 31 WAKEBENCH: Towards a protocol for wind farm flow model evaluation. Part 2: Wind farm wake models. *J. Phys. Conf. Ser.* **2014**, *524*, 012185. [CrossRef]
19. MEASNET. Evaluation of Site-Specific Wind Conditions, Version 2. April 2016. Available online: https://www.measnet.com/wp-content/uploads/2016/05/Measnet_SiteAssessment_V2.0.pdf (accessed on 1 April 2021).
20. International Electrotechnical Commission. IEC 61400-12-1:2017 ed2. Wind Energy Generation Systems—Part 12-1: Power Performance Measurements of Electricity Producing Wind Turbines. Available online: https://webstore.iec.ch/publication/26603 (accessed on 1 April 2021).
21. Uchida, T. Numerical Investigation of Terrain-Induced Turbulence in Complex Terrain by Large-Eddy Simulation (LES) Technique. *Energies* **2018**, *11*, 2638. [CrossRef]